On the dynamics of current jets trapped to the flanks of mid-ocean ridges

J. W. Lavelle[1]

Received 26 September 2011; revised 23 May 2012; accepted 23 May 2012; published 6 July 2012.

[1] Time-mean abyssal current observations over the flanks of the East Pacific Rise (EPR) at 9–10°N and at the Juan de Fuca Ridge at 45°N document the occurrence of paired along-ridge current jets that are trapped to the ridge flanks and sheared across the ridge in an anticyclonic sense. A coincident feature, where local hydrothermal discharge effects are not in play, is the upward bowing of isopycnals over ridge crests and isopycnals plunging into ridge flanks. It would be tempting to explain the jets primarily as geostrophic responses to the doming/plunging isopycnal distribution, though that should lead to the question as to how the isopycnal perturbations originate. A numerical model of time-dependent flow on a cross-ridge (x–z) transect, forced in a way to be consistent with a yearlong, hourly sampled record of currents measured at the EPR ridge crest, is used to investigate some of the underlying physics. It will be shown that the jets can arise from oscillatory flows via eddy-momentum, eddy-heat, and eddy-salt fluxes that ultimately cause the isopycnals to dome over the ridge. As the probable offspring of velocity-velocity and velocity-density correlations that depend upon oscillatory motion, the jets are likely examples of stratified topographic flow rectification. An ancillary feature is a slight yearlong-averaged downward current O (0.1–0.5 mm/s) over the EPR ridge crest that crosses the time-mean, upward bowing isopycnals in a counter-intuitive vertical direction.

Citation: Lavelle, J. W. (2012), On the dynamics of current jets trapped to the flanks of mid-ocean ridges, *J. Geophys. Res.*, *117*, C07002, doi:10.1029/2011JC007627.

1. Introduction

[2] Current meter observations at the Juan de Fuca Ridge (JdFR) [e.g., *Thomson et al.*, 1990] and at the East Pacific Rise (EPR) at 9–10°N, both tectonic ridge spreading center sites 2200–2600 m deep in the northeastern Pacific, show long-term mean flows on ridge flanks that are poleward to the west of the crest and equatorward to the east [*Cannon and Pashinski*, 1997; *Adams*, 2007; *Thurnherr et al.*, 2011]. In the first set of observations cited, currents were measured at a single (ridge-crest) depth level and their means (3 month) showed ridge-parallel anti-cyclonically paired mean flows with speed maxima of ~3 cm s^{-1} at 5–10 km off axis that all but disappeared between 15 and 25 km each side of the ridge. Earlier *Cannon et al.* [1991] had shown with just a few progressive vector trajectories that long-period flow could be along and anti-cyclonically sheared across the same ridge. *Helfrich et al.* [1998] added flow data from the depth of the JdFR crest to 1800 m and showed that these mean flows were of limited vertical extent above crest depth as well. *Thurnherr et al.* [2011] showed the presence of ridge-trapped jets at the EPR 9–10°N using repeated lowered Acoustic Doppler Current Profiler (ADCP) and moored current observations. *Thurnherr et al.*'s [2011] moored current profiler at ~10 km west of the EPR showed, for example, that beyond a possible bottom boundary effect, these mean flows were strongest between 2600 m and the seafloor, and their weekly averaged intensities varied greatly. The numerical models of *McGillicuddy et al.* [2010] in 2-D and *Lavelle et al.* [2010] in 3-D further defined the character of ridge-trapped along-ridge flows (jets) while descriptively connecting them to the time-dependent regional flow at the EPR. *McGillicuddy et al.* [2010] showed the importance of the jets in the transport of hydrothermally supported larval species. This paper returns to the phenomenon of the jets to examine their underlying physical dynamics.

[3] Flow near the ridges cannot be divorced from ridge hydrography. *Cannon et al.* [1991], *Cannon and Pashinski* [1997], and *Thurnherr et al.* [2011] all showed isotherms/isopycnals that dome over the ridge crests. Isotherms/isopycnals plunging into ridge flanks are also observed, though not necessarily symmetrically about the ridge crest. Isopycnals uplifted on one side and down-set of the other side of the crest are likely evidence of cross-ridge flow. Isotherms/isopycnals have also been observed to plunge directly into the ridge crest rather than dome above it [*Crane et al.*, 1985; *Helfrich et al.*, 1998]. Those transects can be interpreted as showing effects of hydrothermal heat vented at the ridge crest. The model used here does not incorporate hydrothermal heat

[1]NOAA/Pacific Marine Environmental Laboratory, Seattle, Washington, USA.

Corresponding author: J. W. Lavelle, NOAA/Pacific Marine Environmental Laboratory, 7600 Sand Point Way NE, Seattle, WA 98115, USA. (j.william.lavelle@noaa.gov)

flux effects because hydrothermal sources are isolated and relatively sparse along ridges, and the focus is on the more general ridge-jet problem.

[4] Spectra of observed currents at both JdFR and EPR sites show substantial subinertial frequency components [*Cannon et al.*, 1991; *Lavelle et al.*, 2010]. At the JdFR, the subinertial band (T > ~17.2 h) of observed currents includes the diurnal tidal currents and a pronounced broad spectral peak at three to eight days [*Cannon and Thomson*, 1996]. At the EPR ridge *crest*, the subinertial band (T > ~73 h) of observed currents contains more than one third of the spectral kinetic energy (KE), with the most prominent sub-inertial spectral peak occurring near 42 days. In the *far field*, however, the KE in the subinertial band, based on model inference, is only 9.4% of the total KE. At EPR 9–10°N, diurnal and semidiurnal tidal frequencies are both super-inertial and thus internal wave producing.

[5] Some of the earliest work on oscillatory/residual flow over topography in a rotating environment concentrated on the effects of tidal rather than subinertial forced flows, and in shallow environments where stratification was negligible and bottom friction was not [e.g., *Huthnance*, 1973; *Tee*, 1976; *Loder*, 1980; *Robinson*, 1981]. A separate but related line of investigation, exemplified by the work by *Bretherton and Haidvogel* [1976], has looked at residual flow following the unforced interaction of random eddy fields with topography. In the tidally forced cases, residual flows were said to result from the process of "tidal rectification," a subcategory, when other forcing frequencies are considered, of the broader classification "topographic rectification." Lateral form variation, (e.g., inlets [*Imasato*, 1983]), variable bottom topography, or both can cause topographic rectification. *Zimmerman* [1980] and *Maas and Zimmerman* [1989] among others expanded early rectification analysis by adding stratification. While stratification is not essential to rectification, stratification typically localizes and intensifies the resulting residual flows. Since those early, mostly analytic treatments, flow rectification as one outcome of oscillatory motion over undulating or otherwise variable bathymetry in both stratified and unstratified environments (e.g., shelves/slopes, seamounts, and submarine banks) has been a subject of numerous studies [e.g., *Garreau and Mazé*, 1992; *Shen and Thompson*, 1997; *Pérenne et al.*, 2000; *Chen et al.*, 2001; *Mohn et al.*, 2009; *Brink*, 2010].

[6] The modeling work of *Chen and Beardsley* [1995], which examined tidal rectification over Georges Bank, may come closest to the nature of the calculation reported here. Differences in this and their problem configuration and model numerics are still substantial: depth and shape of topography, stratification, latitude (rotation rate), forcing (their tidal versus the present wide spectrum of frequencies), model boundary conditions, model grid structure, etc. Still, a number of analogous features in their and the present results occur, on which comments will be made later. Later *Beckmann and Haidvogel* [1997] modeled mean circulation at Fieberling Guyot caused by impinging tidal currents and examined the contributions of individual terms in the governing equations, as *Chen and Beardsley* [1995] did and as is done here.

[7] In this paper, the focus is on the dynamic and kinematic balances that result in rectified flow along the flanks of mid-ocean spreading center ridges. One substantial difference with models mentioned earlier is that a wide spectrum of oscillatory motions, taken from a yearlong record of currents measured hourly at the EPR, is used to force the flow. While the focus is on yearlong averages, some shorter term average results will be given to demonstrate, among other things, that dynamical balances change with the averaging interval and to re-make the point that the phrase "time average" should always be accompanied by specification of the time interval over which the average was made. Factors that will influence the details of rectified flow at any one location include the ridge latitude (via the Coriolis force), the ridge shape and depth, the local stratification, and the spectrum of the impinging currents. It is not a goal here to explore all those dependencies, but only to elucidate by example the fundamental processes/balances that maintain these narrow jets that are so important to the transport of fluid and material along spreading center ridge topography [e.g., *McGillicuddy et al.*, 2010].

2. Model Configuration

[8] The numerical model employed here is two-dimensional and time-dependent; it is a baroclinic, hydrostatic, free-surface, z-level, and f-planar primitive equation construct, a dimensionally reduced implementation of the 3-d model described in *Lavelle* [2006] and *Lavelle et al.* [2010]. The primary variables of the equation set are u, v, and w velocities in x, y, and z directions; η, the sea surface elevation; θ, S, and ρ, the potential temperature, salinity, and density via an equation of state. Viscous and diffusive mixing terms are Laplacian (e.g., equation (1)), with time- and space-dependent horizontal and vertical viscosity and diffusivity coefficients that independently depend on velocity shears and stratification [*Smagorinsky*, 1993]. A domain-perimeter sponge [*Lavelle and Thacker*, 2008] makes the model boundaries open to incoming forcing and outgoing internal waves. The model ridge was taken to be oriented in the north–south direction and its bathymetry was assumed to be invariant along that direction. The invariance assumption, save for a meridional sea-surface gradient for forcing (equation (2)), was made so that important mechanisms of the along-ridge flow dynamics could be more clearly described. However, an infinitely long ridge rather than a ridge segment eliminates the possibility of trapped wave resonances of the kind described by, e.g., *Brink* [1989] for more circular geometries and whatever residual flow those waves may support. Furthermore, disallowing along-ridge bathymetric variations, whether for an infinitely long ridge or a ridge segment, rules out the possibility of additional residual flow from the mechanism described in *Haidvogel and Brink* [1986] and re-examined in *Brink* [2010]. The model used here is nearly identical to that of *McGillicuddy et al.* [2010], though their work was directed not at flow dynamics but at understanding larval transport along an EPR-like ridge. *McGillicuddy et al.*'s [2010] model centered on a shorter (7 month) and earlier (1999) time interval and used a different bathymetric profile.

[9] Model bathymetry here is based on depth observations gridded to 241 m × 241 m resolution and archived at the Lamont-Doherty Earth Observatory. Depth values averaged over latitudes 9.55–9.6°N out to 150 km both sides of the ridge crest show values declining from a minimum of

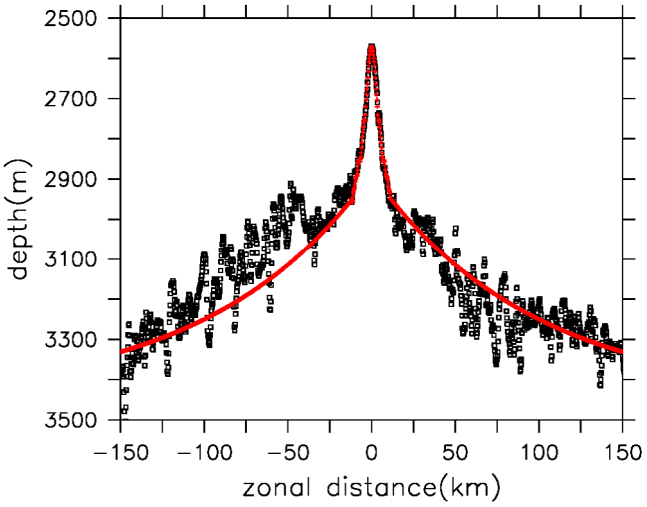

Figure 1. Gridded bathymetry of the EPR at 241 m horizontal resolution was acquired from the Lamont-Doherty Earth Observatory archives (http://www.ldeo.columbia.edu/research/marine-geology-geophysics/ridge-multibeam-bathymetry-synthesis). Boxes represent those data averaged over latitudes 9.55–9.6°N. The peak (2570 m) on this transect corresponds to longitude 104°15.22′W. For use in the model, the bathymetry was approximated by the superimposed axially symmetric (red) curve.

2570 m at the crest to approximately 3350 m at 150 km from the crest (Figure 1). These data were then approximated by a ridge-symmetric analytic curve (Figure 1, red curve) that was then clipped to have a depth maximum at 3300 m.

[10] Model hydrography is based on profile data taken during the October–November 2006 LADDER (Larval Dispersal on the Deep East Pacific Rise) expedition to the EPR [*Thurnherr et al.*, 2011]. An ensemble average of four of those profiles provided the initial model θ and S fields and subsequent boundary constraints (per *Lavelle et al.* [2010]). Variables θ and S were nudged back to their initial values (with time constant of 6 h) over the near-surface 200 m of the water column. This small change to earlier model applications provides enhanced compensation for near-surface processes, which, with the model's focus on abyssal flow, have not been included. The absence of sufficient site data disallowed specifying a seasonally variable far-field hydrography, though at ridge-crest depths along the EPR, little seasonal variability of θ and S should be expected.

[11] Model forcing, equivalent to a regional sea surface gradient, was taken to be spatially uniform over the domain. Its time dependence was derived using an iterative inverse calculation designed to make model-estimated and measured currents match at the ridge crest. The calculation postulates that currents at any point in the model domain result from a convolution in time of a function representing the model and a far-field forcing current time series. The convolution theorem then is used to relate the Fourier component amplitudes, input $I(\omega)$ and output $O(\omega)$, of their respective time series via a model transfer function $M(\omega)$ at each oscillation frequency (ω) for any spatial location. A far-field test input time series I_1 and the model output time series O_1 at a specific point, i.e., one field-measurement location, are thus related through $M(\omega)$: $O_1(\omega) = M(\omega) \times I_1(\omega)$. An 'ideal' far-field input time series I_2 and an actual measured time series O_0 would also be related through $M(\omega)$: $O_0(\omega) = M(\omega) \times I_2(\omega)$. Eliminating $M(\omega)$ from the two frequency-space equations yields $I_2(\omega) = O_0(\omega) \times I_1(\omega) / O_1(\omega)$. The spectrum $I_2(\omega)$ then provides a better estimate of a far-field current time series for use in forcing. The estimation cycle can be, and in this case was, repeated as an iteration. Discussion of finer points in the estimation of the 'ideal' input series and examples of the efficacy of the method can be found in *McGillicuddy et al.* [2010] and *Lavelle et al.* [2010]. For the present process study, the importance of this method lies in its creation of a credible [*McGillicuddy et al.*, 2010] forcing time series specifically of abyssal currents containing a multitude of frequencies.

[12] Hourly data over the time period November 2006 into November 2007 (Meter C-2440 m [*Thurnherr et al.*, 2011]), a time series of 383.5 days in length, led to the derived far-field time series used to force the model. The length of 383.5 d was chosen because it is a whole number multiple of a lunar cycle (~29.5 d); hereafter, "year-long" will surrogate for 383.5 d. The spectrum of the derived far-field current time series has power at periods ranging from 2 h to steady flow. Results are consequently not biased by preconceptions of what frequencies should be important to the outcome. The correlation coefficients (r) between measured and inverse-derived ridge-crest currents for u and v components after the final iteration were 0.95 and 0.93, respectively. The far-field (u, v) time means, (1.6, −2.4) mm s^{-1} by iteration inference, were set identically to zero for the experiments reported here. *Lavelle et al.* [2010] reported that the measured crest currents had a KE distribution such that semidiurnal, long period (T > 200 h), inertial, and diurnal band motions accounted for 35%, 35%, 14%, and 4%, respectively. The small amount of energy at frequencies higher than semidiurnal (10%) makes the hydrostatic approximation for the model reasonable [e.g., *Zaron and Egbert*, 2006; *Mahadevan*, 2006].

[13] Model equations were discretized over finite volumes on a z-level C grid stretched in both horizontal and vertical directions. The analytic representation of bathymetry (Figure 1) was discretized using those fixed z-levels. Using full grid cells to represent bathymetry causes minor vertical striations at bathymetric step risers in some of the diagrams to follow. The 'shaved-cell' method of *Adcroft et al.* [1997] could reduce that step effect, but it has not yet been implemented in the numerical code used for this work. Narrow zones near the open lateral boundaries contained the "pretty good sponge" of *Lavelle and Thacker* [2008] through which incoming motions and outgoing internal waves efficiently pass. Spatial grid size was typically 265 × 128 in x (zonal) and z (depth) directions, with finest resolution at the ridge crest of 440 m horizontally and 14 m vertically. The integration time step was of 75 s, so that each yearlong experiment plus 30 d spin-up period required 476,000 time steps. Variable fields were recorded at 2 h intervals over an entire experiment's duration (383.5 d) and, from those, averages were calculated. In addition, all terms in the momentum equations and all terms in the heat and salt transport equations were archived at the same time so that momentum and property flux balances could be examined. The model experiments reported here encompass a base experiment in which all possible spectral components of the forcing

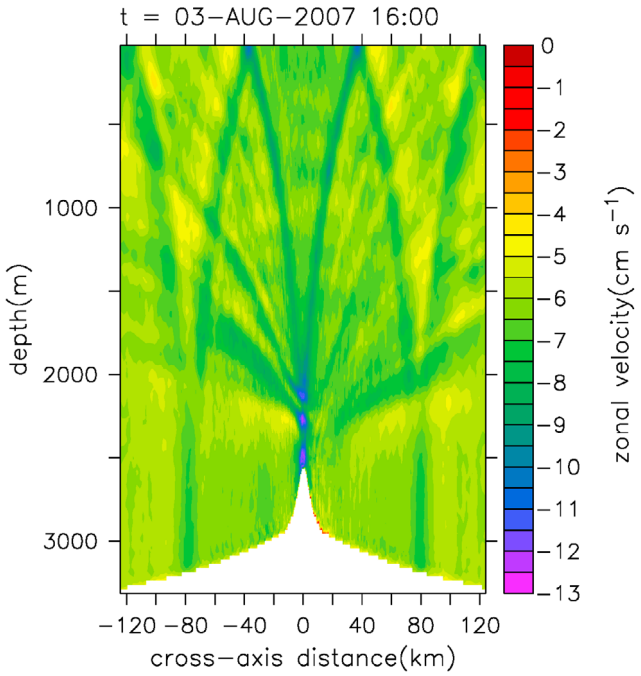

Figure 2. Zonal velocity over an axially symmetric EPR-like ridge at an instance 7336 h into the simulation. The model forcing time series contains several thousand wave frequencies in the internal wave (IW) band. Results show no indication of significant internal wave reflection at the domain edges after thousands of simulated hours.

determined the outcome, and three experiments in which different sub-inertial intervals of the spectra were deleted. Greater detail on the physics and numerics of the model can be found in *Lavelle* [2006] and *Lavelle et al.* [2010].

[14] Flow steered by topography has an extensive history of investigation (one entry to the literature is *Brink* [2010, and the references therein]). An alternative to the primitive equation approach for modeling the effects of topography on flow begins with the potential vorticity (PV) equation [e.g., *Bretherton and Haidvogel*, 1976; *Müller*, 1995; *Ou*, 1999]. Examples of the PV approach applied to elongated topographic features are found in papers by *Vallis and Maltrud* [1993], who examined the formation of jets over ridges, and *Zimmerman* [1978], who studied tidally induced residual flows over irregular topography, both under homogeneous flow conditions. *Andersson and Veronis* [2004] examined circulation with stratification over a mid-ocean ridge using a two-layer PV model. The PV equation originates in the primitive equations, so PV and primitive equation approaches provide equivalent but alternative strategies for studying topographically controlled flow.

3. Model Results and Discussion

[15] Forming the bases of the mean fields are the instantaneous fields, the temporal averages of which reveal the dynamics of the ridge-trapped residual flows. Those instantaneous model fields are replete with internal wave (IW) motions [e.g., *Garrett and Kunze*, 2007], as exemplified in a snapshot of instantaneous zonal flow (u) across the ridge taken at an arbitrary time of 7336 h into the simulation (Figure 2). Because the M_2 is the most energetic observed spectral line in the frequency band (~1 h < T < 72.7 h) supporting internal waves at this latitude (9.5°N), it is the most prominent but not the only wave ray in evidence in Figure 2. Note, however, that differences between actual and model stratification near the sea surface as well as the imposed cross-ridge bathymetric symmetry make this IW field somewhat idealized. Nonetheless, instantaneous u is likely to be nearly always significantly amplified in the region several hundred meters above the ridge crest with respect to its value in the far field (Figure 2). This is also a region of elevated horizontal velocity shear that, in turn, leads to enhanced turbulent mixing [e.g., *Lavelle*, 2006].

[16] The ridge-trapped flank jets are most clearly defined in the yearlong average of meridional flow (Figure 3). Using the 1 cm s^{-1} contour value as an edge, the flow extends as much as 275 m above the ridge crest, and as much as 17 km to the west and 13 km to the east of the ridge axis at crest depth. Flow is trapped far down the sides of the flanks reaching a water depth of ~3000 m, some 425 m below the ridge crest. In this northern hemisphere example, the jets are poleward on the west and equatorward to the east of the ridge. Over this long averaging interval, the westward and eastward jets are of comparable cross-sectional size and have nearly equal speed maxima (4.6 cm s^{-1} and 4.1 cm s^{-1}). The speed maxima in this quasi-idealized case are somewhat higher than the ~3 cm s^{-1} 3-month average maxima measured across the JdFR [*Cannon and Pashinski*, 1997]. Figure 3 shows the speed maxima lie below ridge-crest depth, a depth region that *Cannon and Pashinski* [1997] did not sample. Fluxes poleward and equatorward within the 1 cm s^{-1} contour are 0.23 and −0.12 Sv, respectively. Anticyclonic azimuthal flows trapped to the summit and

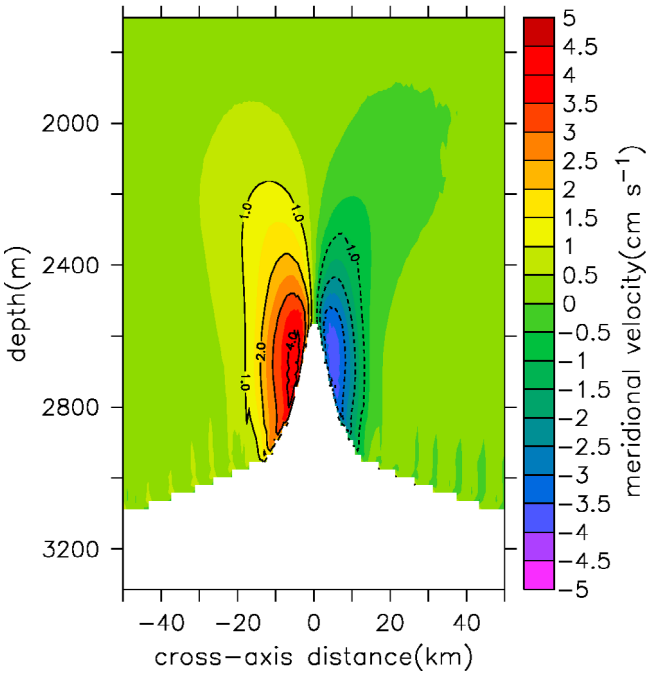

Figure 3. Meridional velocities averaged over 383.5 days. Line contours every whole number cm s^{-1} are superposed.

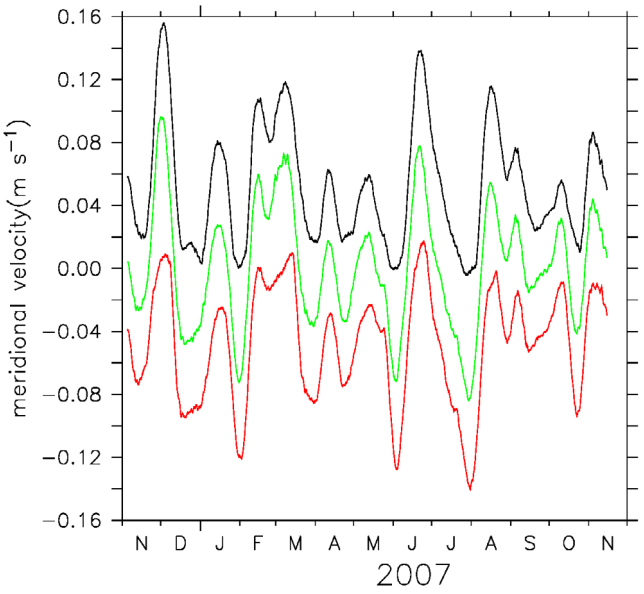

Figure 4. Time variations of the extremal velocity in each jet after averaging instantaneous meridional currents over 100 h using a box-car window. Black is the poleward flow; red is the equatorward flow; green is the velocity at 100 m above the center point of the ridge. The most prominent oscillation periods in these series occur between 40 and 50 d.

upper flanks of submarine banks [e.g., *Chen and Beardsley*, 1995] and seamounts [e.g., *Brink*, 1995; *Beckmann and Haidvogel*, 1997; *Lavelle and Mohn*, 2010] share similar dynamical origins.

[17] The jets depicted in Figure 3 exhibit significant subtidal variations. The maximum and minimum velocities in the core of the jets, west and east of the ridge respectively, are plotted in time (Figure 4) after model results were box-car averaged over a period of 100 h to isolate the subinertial variability. The most prominent oscillations in Figure 3 occur at a periods of 40–50 d. The cause of this periodicity is still to be settled, though *Adams et al.* [2011] offer one possibility. These same time series show that maximum poleward and minimum equatorward currents can reach speeds of as much as 15 cm s^{-1}. The middle curve in Figure 4 shows the maximum meridional velocity on axis. That time series crossing zero multiple times shows that the interface between the jets sweeps alternatively back and forth across the ridge axis, as *McGillicuddy et al.* [2010] reported. Net meridional flow 100 m above the ridge axis <v (x = 0, z = 2470 m) >over this yearlong period was poleward at 0.26 cm s^{-1}.

[18] Distributions of the yearlong averaged θ anomaly, $\langle\Delta\theta\rangle$, (Figure 5a, in color), potential density anomaly $\langle\sigma_0\rangle$ (Figure 5a, line contours), and vertical flow $\langle w\rangle$ (Figure 5b) are essential to understanding the underlying dynamics. Here $\langle\Delta\theta\rangle$ is θ–$\theta_{\text{FAR-FIELD}}$ both evaluated at the same depth. The $\langle\Delta\theta\rangle$ distribution (Figure 5a) shows a region of anomalously cold water, a cold dome, extending upward above the ridge crest to at least 1800 m depth. The $\langle\Delta\theta\rangle$ minimum is nearly −0.02°C. A smaller region of anomalously warm water hugs the lower flanks of the ridge crest. The salinity anomaly (ΔS, not shown) is positive over the ridge crest and negative on the ridge flanks. ΔS and $\Delta\theta$ are partly compensating with respect to density, but not enough to prevent $\langle\sigma_0\rangle$ from being uplifted over the ridge crest and set down on the ridge flanks (Figure 5a, contours).

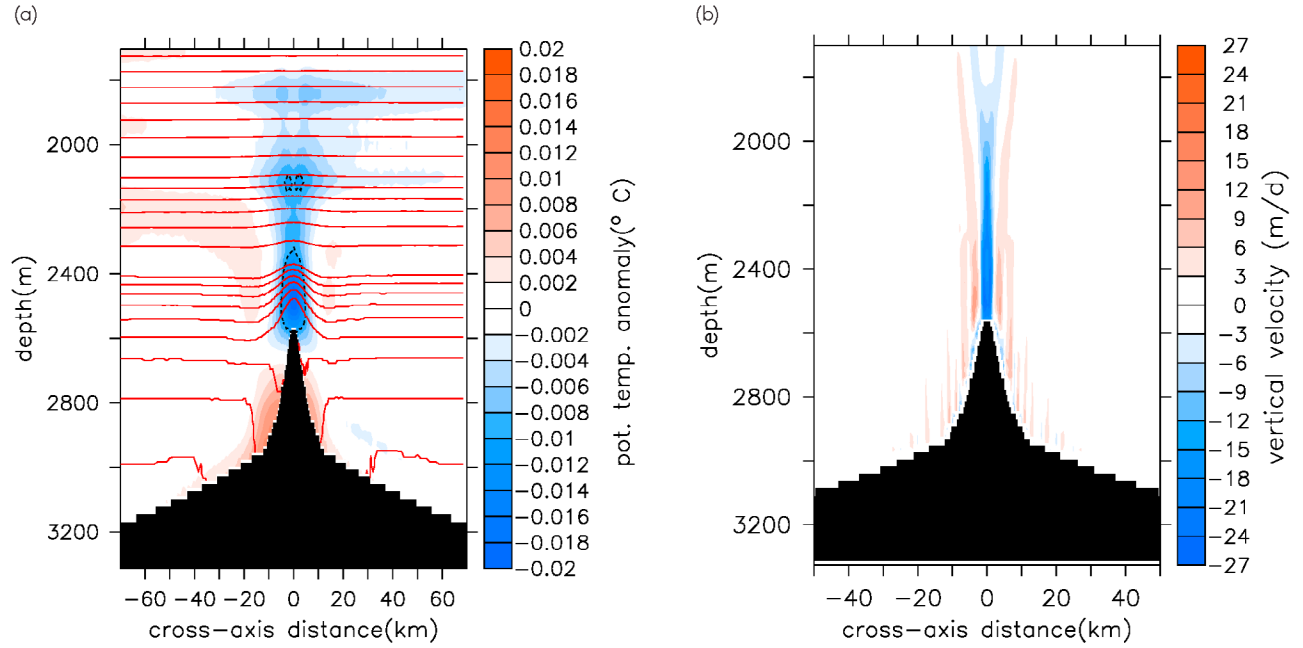

Figure 5. (a) The yearlong average of $\Delta\theta$ contoured in color, with blue indicating an anomalously cold region. Dash black lines circumscribe regions of negative anomalies >0.01°C. Superposed solid line contours represent σ_0 over the range of 27.62 to 27.74 kg m^{-3}. For clarity of presentation, σ_0 contours are not uniformly spaced. (b) The yearlong average and zonally windowed (5-cell Hanning) vertical velocity in units of m d^{-1}.

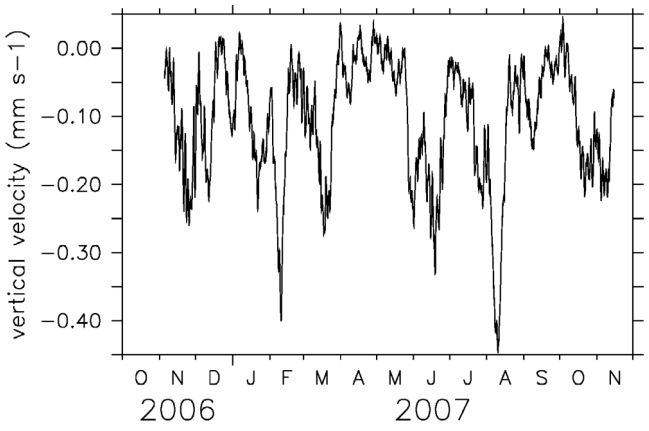

Figure 6. Vertical velocity directly over the ridge crest at 2500 m depth as a time series, after smoothing with 100 h boxcar window to suppress tidal variations.

[19] The yearlong-average vertical velocity ⟨w⟩ (Figure 5b) is downward over the ridge crest and upward to both sides of that downward flow. The time series of w at 2500 m depth right over the ridge, after smoothing with a 100 h boxcar window, shows vertical flow to have considerable temporal variability (Figure 6). The yearlong mean ⟨w⟩ at 2500 m depth is 0.1 mm s^{-1} downward. For brief times, however, flow can be upward, or as large as 0.5 mm s^{-1} downward. Vertical currents above any ridge crest have yet to be observed, though *Brink* [1995], for example, inferred downward flow with a magnitude about 4 times this size over Fieberling Guyot.

[20] The two juxtaposed yearlong-mean fields (Figures 5a and 5b) immediately present these puzzles: How can $\langle\sigma_0\rangle$ contours be bowed upward when ⟨w⟩ is directed downward, crossing $\langle\sigma_0\rangle$ contours? *Brink* [1995] also flagged this conundrum. The answers are postponed until the effect of the upward bowing isopycnals on meridional flow is elucidated.

[21] A subset of the model equations, written in unstretched coordinate form for discussion sake, provides the framework for addressing the important dynamical balances

$$\frac{\partial u}{\partial t}+\frac{\partial(uu)}{\partial x}+\frac{\partial(uw)}{\partial z}=+fv-g\frac{\partial\eta}{\partial x}-\frac{1}{\rho_0}\frac{\partial p'}{\partial x}+\frac{\partial}{\partial x}A_h\frac{\partial u}{\partial x}+\frac{\partial}{\partial z}A_z\frac{\partial u}{\partial z}-\alpha(u-u_{BKG}), \quad (1)$$

$$\frac{\partial v}{\partial t}+\frac{\partial(vu)}{\partial x}+\frac{\partial(vw)}{\partial z}=-fu-g\frac{\partial\eta}{\partial y}+\frac{\partial}{\partial x}A_h\frac{\partial v}{\partial x}+\frac{\partial}{\partial z}A_z\frac{\partial v}{\partial z}, \quad (2)$$

$$\frac{\partial u}{\partial x}+\frac{\partial w}{\partial z}=0. \quad (3)$$

[22] The first two are the momentum equations for the zonal (cross-ridge) velocity (u) and meridional (along-ridge) velocity (v). The third is the continuity equation. All y derivatives are zero per the model assumption of along-ridge invariance, except for the y-gradient of the sea surface that acts to force the motion. In equations (1)–(3), w is the vertical velocity, f the Coriolis parameter, g the acceleration of gravity, η is the sea-surface height, ρ_0 is the reference density, p′ the pressure resulting from a θ, S dependent density (the baroclinic component), and A_h and A_z are time- and space-dependent horizontal and vertical viscosities, respectively. The sponge coefficient α, nonzero only at distances greater than 125 km from the ridge crest in this example, has no role in balances where jets occur.

[23] Time-averaged, restricted to the unsponged region, and regrouped, equations (1) and (2) are

$$\left\langle\frac{\partial u}{\partial t}\right\rangle=-\left[\frac{\partial\langle uu\rangle}{\partial x}+\frac{\partial\langle uw\rangle}{\partial z}\right]+f\langle v\rangle-g\frac{\partial\langle\eta\rangle}{\partial x}-\frac{\partial\langle p\rangle}{\partial x}+\left\langle\frac{\partial}{\partial x}A_h\frac{\partial u}{\partial x}\right\rangle+\left\langle\frac{\partial}{\partial z}A_z\frac{\partial u}{\partial z}\right\rangle, \quad (4)$$

$$\left\langle\frac{\partial v}{\partial t}\right\rangle=-\left[\frac{\partial}{\partial x}\langle uv\rangle+\frac{\partial}{\partial z}\langle wv\rangle\right]-f\langle u\rangle-g\frac{\partial\langle\eta\rangle}{\partial y}+\left\langle\frac{\partial}{\partial x}A_h\frac{\partial v}{\partial x}\right\rangle+\left\langle\frac{\partial}{\partial z}A_z\frac{\partial v}{\partial z}\right\rangle, \quad (5)$$

where the ⟨⟩ represents time averaging. Both equations must be identically satisfied at every point in the unsponged model domain.

[24] When the terms in equation (4) are evaluated at a single depth level just above crest depth and averaged over a year, results have the form shown in Figure 7a. In the yearlong averages and within 20 km each side of the ridge where the jets are prominent (Figure 3), only three terms are significant in defining the momentum balance of equation (4): the Coriolis, the baroclinic pressure gradient, and the nonlinear advection terms. The time rate of change and viscous terms (equation (4)) are several orders of magnitude smaller than the others. Over most of the nearest 20 km each side of the ridge, the balance is primarily between Coriolis and baroclinic pressure gradient terms, i.e., the balance is primarily geostrophic (Figure 7a). The nonlinear advective terms are of significant size in the mean only out to ∼3 km on both sides of the ridge. Within that ±3 km near-ridge zone, however, nonlinear advection matches the magnitude of the baroclinic pressure gradient so that close to the ridge at this depth the forces are not in geostrophic balance. A transect view of these same cross-ridge forces is presented in Figure 8. These force diagrams, however, do not reveal the importance of the nonlinear momentum terms during the spin-up period out of which eventual along-ridge distributions come.

[25] When the averaging period is shortened to 29.5 days (Figure 7b), the $\langle\partial u/\partial t\rangle$ term, though still small, is no longer negligible. The principal difference between this and Figure 7a is that the force terms are much larger on the east side of the ridge than the west. During this shorter averaging interval, the equatorward jet on the east side of the ridge was strongest. The net zonal flow during these 29.5 days was eastward. The corresponding hydrography distribution (not shown) is ridge-crest asymmetric, with upward bowed isopycnals on the west side and downward displaced isopycnals to the east of the ridge, and the isotherm dome center displaced eastward as well [*Lavelle et al.*, 2010]. The largest terms in the force balance remain the Coriolis and baroclinic pressure gradient terms, with the nonlinear advection terms still small except in the several kilometers nearest the ridge axis. Note that the crossover point for the baroclinic pressure gradient to reverse sign is to the west of the ridge crest. As is

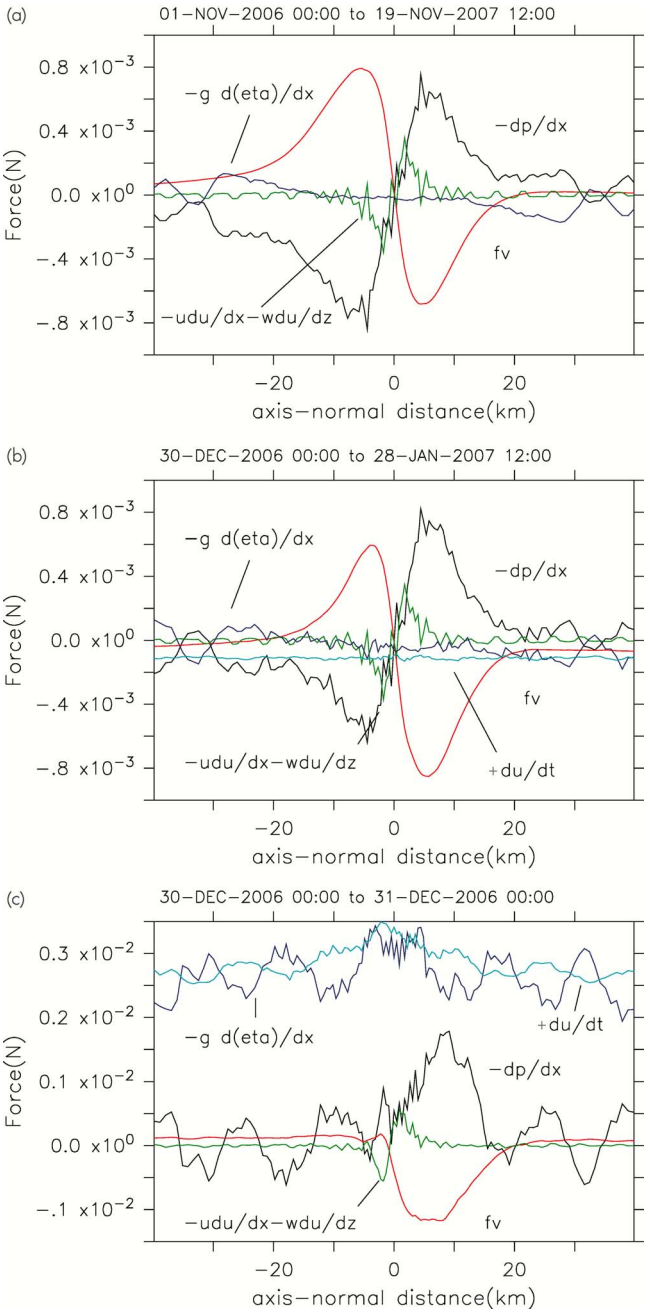

Figure 7. Terms in the u-momentum equation at 2500 m depth, 70 m above the ridge crest: Coriolis (red), baroclinic pressure gradient (black), nonlinear advection (green), barotropic pressure gradient (sea surface height gradient, blue), time rate of change (cyan). (a) A yearlong average, (b) a 29.5 day average, and (c) a 1 day average. Viscous terms in equation (4) are negligible at this ordinate scale in all cases. The nonlinear term in Figure 7a can be considered the eddy flux term as the steady component of the term is negligible. Averaging periods for Figures 7b and 7c are indicated above each figure. Differentials in the labels are all partial differentials.

true in Figure 7a, it would be wrong to characterize the force balance within ~4 km either side of the ridge crest as being geostrophic.

[26] When the time average is reduced to a single day, the *barotropic* pressure gradients and $\langle \partial u/\partial t \rangle$ terms are largest and nearly balance one another (Figure 7c). The nonlinear advection terms are miniscule in this case, and while the baroclinic pressure gradient and Coriolis terms are of nearly opposite size over the inner ±15 km of the ridge crest, the overall force balance is dominated by time acceleration and surface pressure gradient terms. This diagram, representative of one-day averages, raises the question as to whether snapshot hydrography over abrupt topography should ever be used to evaluate local ocean currents under a geostrophic balance assumption.

[27] Force balances in the along-ridge direction (equation (5)) are shown in Figure 9. In an annual average, the balance is primarily between the Coriolis and nonlinear advection, with a general sense, based on the Coriolis force term of divergent off-ridge flow at the depth level (z = 2500 m) shown. When integrated over the entire water column, eddy-momentum flux and bottom stress are the principal terms in the yearlong momentum balance in the along-ridge direction [e.g., *Huthnance*, 1973], with a minor contribution to the balance coming from lateral viscous mixing. By construction, no along-ridge baroclinic pressure gradient was allowed. The ordinate scaling in Figure 9a is 50 times less that in Figure 7a, so the maximum off-axis zonal flow at this depth is ~0.1 cm s^{-1} based on values in Figure 3. An analogous diagram at 2300 m depth shows, via the Coriolis force term, that zonal flows are converging to the ridge crest location at that level. More generally, convergent-divergent zonal flows near ridge-depth couple with the downward yearlong mean vertical flow (Figure 5b) to create two slow vertical recirculation cells, each having an opposite circulation sense, one on each side of the ridge. An analogous circulation cell cylinder over Fieberling Guyot was inferred from observations by *Brink* [1995] and from the model results by *Beckmann and Haidvogel* [1997]. At any smaller averaging time interval (Figures 9b and 9c), all four terms shown enter into determining the forcing balance.

[28] The progression of balances in Figures 7 and 9 shows that the time-averaging interval very much changes which terms in the momentum equations are the most significant. Problem definition does the same. In the rectification study of *Huthnance* [1973] of very strong semi-diurnal tidal flow over shallow water sands waves, for example, where stratification was not present, the balance of forces (equation (5)), when vertically averaged, occurred between the nonlinear advection terms (gradients of momentum eddy fluxes) and bottom stress. In the much deeper, stratified ocean setting of spreading center ridges, bottom stress is no longer significant in the momentum balances, while the baroclinic pressure gradient looms large in importance (Figure 7a).

[29] If in a yearlong average the ridge jets are primarily (but not exactly, or everywhere) in geostrophic balance with the hydrography, the next question to ask is what causes the hydrography to be uplifted over the ridge crest and plunge into the ridge flanks (Figure 5) in distributions that contribute to jet size and intensity. The equation for the conservation of heat, expressed in terms of potential temperature, θ,

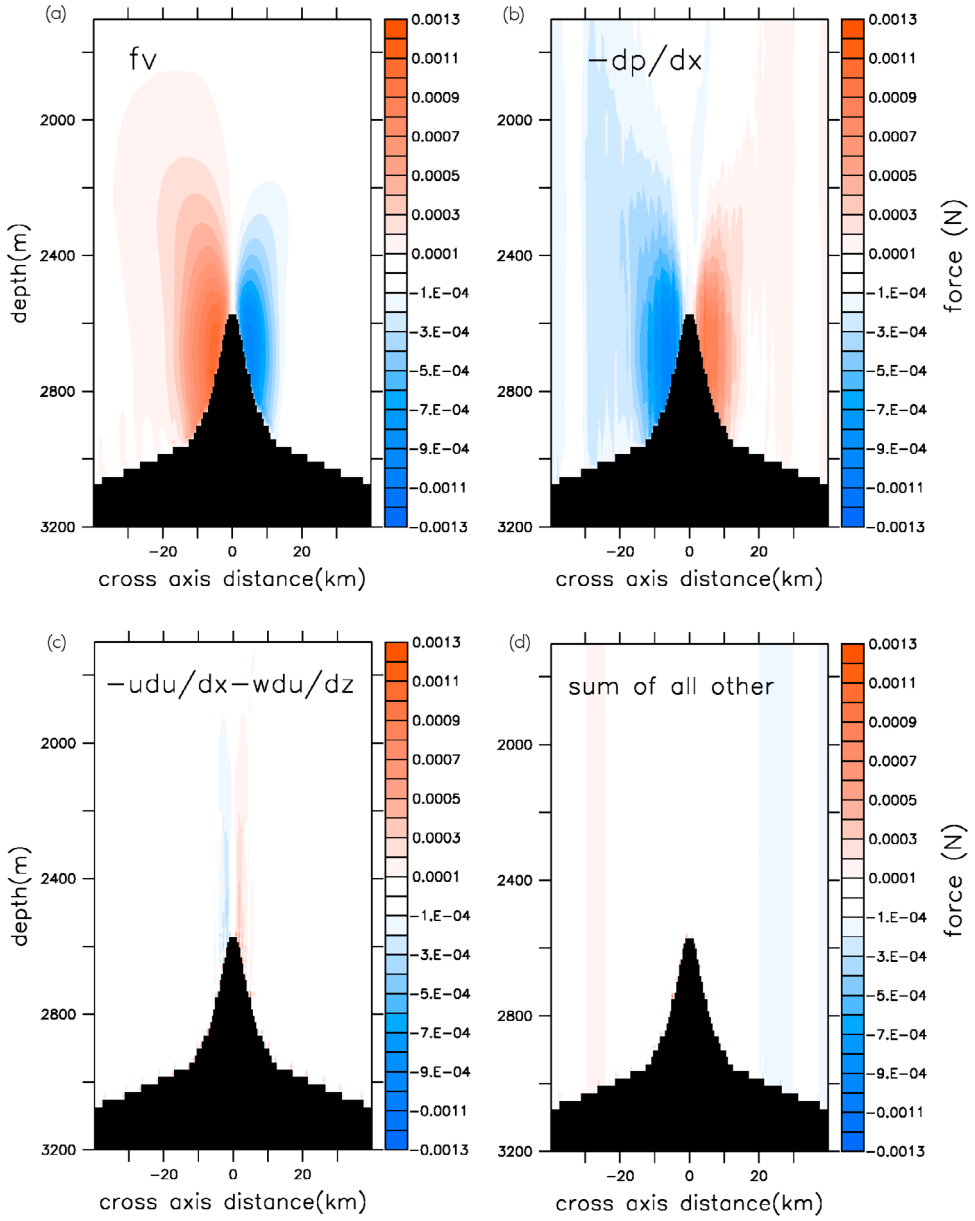

Figure 8. Yearlong averaged force terms (N) in the u-momentum equation (equation (4)) on the same color scale for (a) Coriolis, (b) baroclinic pressure gradient, (c) nonlinear advective terms, and (d) sum of all others. Individually "other" terms making up Figure 8d are all small as well.

under the usual approximations of fixed density and heat capacity, provides the context for the answer

$$\frac{\partial\theta}{\partial t}+\frac{\partial}{\partial x}(u\theta)+\frac{\partial}{\partial z}(w\theta)=\frac{\partial}{\partial x}K_x\frac{\partial\theta}{\partial x}+\frac{\partial}{\partial z}K_z\frac{\partial\theta}{\partial z}-\alpha(\theta-\theta_{BKG}), \tag{6}$$

where K_x and K_z are time- and space-dependent lateral and vertical diffusivities, respectively, and θ_{BKG} is the far-field potential temperature.

[30] When the variables are split into time mean and fluctuating parts

$$\theta=\langle\theta\rangle+\theta',\ u=\langle U\rangle+u',\ w=\langle w\rangle+w',\ K_x=\langle K_x\rangle+K'_x,$$
$$\text{and}\quad K_z=\langle K_z\rangle+K'_z.$$

Equation (6) becomes, after regrouping and restriction to the unsponged region

$$\left\langle\frac{\partial\theta}{\partial t}\right\rangle+\left[\frac{\partial}{\partial x}\langle u\rangle\langle\theta\rangle+\frac{\partial}{\partial z}\langle w\rangle\langle\theta\rangle\right]=-\left[\frac{\partial}{\partial x}\langle u'\theta'\rangle+\frac{\partial}{\partial z}\langle w'\theta'\rangle\right]+\frac{\partial}{\partial x}\langle K_x\rangle\left\langle\frac{\partial\theta}{\partial x}\right\rangle+\frac{\partial}{\partial z}\langle K_z\rangle\left\langle\frac{\partial\theta}{\partial z}\right\rangle+\frac{\partial}{\partial x}\left\langle K'_x\frac{\partial\theta'}{\partial x}\right\rangle+\frac{\partial}{\partial z}\left\langle K'_z\frac{\partial\theta'}{\partial z}\right\rangle. \tag{7}$$

[31] When the $\langle\rangle$ in equation (7) represents a yearlong average, only the large-bracketed terms in this equation have a principal role in the balance, at least in this EPR configuration. The first term and last four terms, and their sum, all

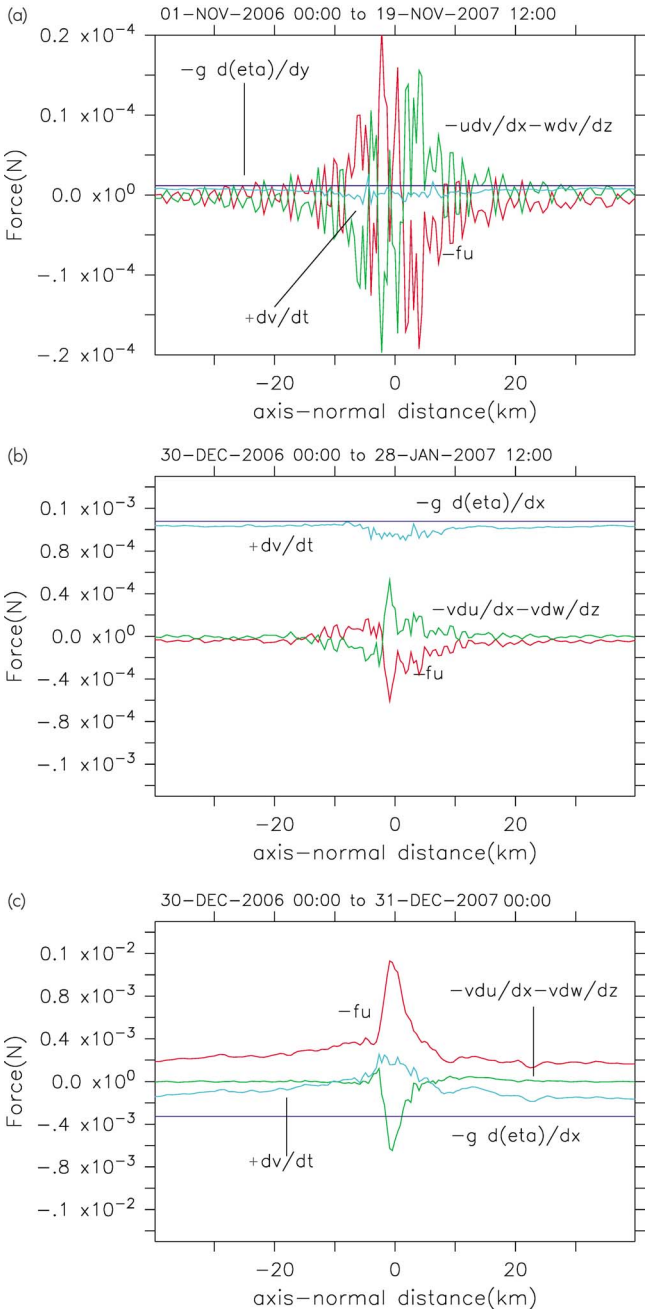

Figure 9. Terms in the v-momentum equation at 2500 m depth, 70 m above the ridge crest: Coriolis (red), nonlinear advection (green), barotropic pressure gradient (sea surface height gradient, blue), and time rate of change (cyan). (a) A yearlong average, (b) a 29.5 day average, and (c) a 1 day average. Viscous terms in equation (5) are negligible at this ordinate scale in all cases. Averaging periods for Figures 9b and 9c are indicated above each figure. Differentials in the labels are all partial differentials.

have distributions whose largest values are several orders less than these large-bracketed terms. Within the first bracket, the two terms are nearly of equal magnitude but of opposite sign. Within the second bracket, the first term is an order of magnitude or more larger than the second term. For Georges Bank, with a much different topography, depth, and forcing, *Chen and Beardsley* [1995] also found that the terms in the first bracket were of comparable magnitude and opposite sign. *Chen and Beardsley* [1995] left it at that, however, without evaluating the distribution of the small difference. The small residual sum of terms in the left hand side large brackets (equation (7)), which is nearly equal to the sum of the two terms in the right hand side large brackets, is the key to understanding the upward bowed isopycnals over the ridge crest. The right hand side large bracket terms can be viewed as a source term, in the sense of Gauss's Theorem [*Morse and Feshbach*, 1953], for the transport equation of the time-mean temperature field. The "source term" in this case is comprised of gradients of the eddy temperature flux.

[32] *Brink* [1995] had earlier sought to identify how the balance in equation (7) was achieved at Fieberling Guyot, but his observational data were not spatially dense enough to do so. *Beckmann and Haidvogel* [1997] found a balance between mean and eddy flux gradients for potential density without any significant contribution at unresolved scales (diffusion), even though their forcing for Fieberling Guyot was limited to diurnal motion.

[33] In the case of this ridge, a good approximation to equation (7) for yearlong averaging period is thus

$$\frac{\partial}{\partial x}\langle u\rangle\langle\theta\rangle + \frac{\partial}{\partial z}\langle w\rangle\langle\theta\rangle \approx -\frac{\partial}{\partial x}\langle u'\theta'\rangle - \frac{\partial}{\partial z}\langle w'\theta'\rangle. \tag{8}$$

[34] Using Q_θ to represent the right hand side of equation (8) and the continuity equation (equation (3)), equation (8) becomes

$$\langle\vec{u}\rangle \cdot \nabla\langle\theta\rangle \approx Q_\theta, \tag{9}$$

where $\vec{u}$ is the time-mean velocity in the direction of the gradient of the time mean θ.

[35] The distribution for the source term Q_θ under yearlong mean conditions is depicted in Figure 10. Q_θ is negative directly above the ridge crest and is thus removing heat from the time mean θ field at those locations (in blue, Figure 10). Q_θ is the source of the negative θ anomalies in Figure 5a, and in consequence time-mean isotherms are domed upward over the ridge crest. Since Q_θ represents the divergence of the positive correlation of oscillating current and oscillating temperature, i.e., the eddy heat flux, the oscillatory fields are what sustain the cold in the "cold dome." An equation analogous to equation (9) could be written for S. When the source Q_S is evaluated in the simulation, Q_S is found to source a positive S anomaly above the ridge crest (not shown).

[36] Since potential density would be well approximated by a linear function of θ and S at depths near the ridge crest, an equation analogous to equation (9) can be written for ρ (or σ_0)

$$\langle\vec{u}\rangle \cdot \nabla\langle\rho\rangle \approx Q_\rho. \tag{10}$$

Q_ρ is nonzero just above the ridge if Q_θ is negative and Q_S is positive there. Since $\nabla\langle\rho\rangle$ is nonzero (Figure 5a), the component of $\langle$(u,w)$\rangle$ in the direction of $\nabla\langle\rho\rangle$ must also be nonzero. Since $\nabla\langle\rho\rangle$ establishes the diapycnal direction, the yearlong mean diapycnal velocity cannot be zero. Furthermore, directly over the ridge crest, the nonzero time-mean diapycnal velocity crosses the upward

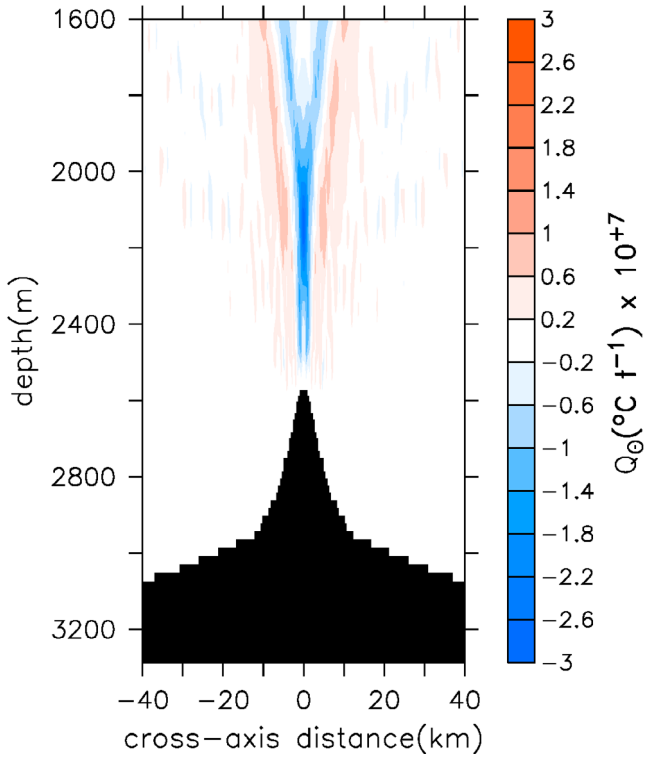

Figure 10. The source term Q_θ (equation (9)) for the yearlong averaged base case.

bowing time-mean isopycnals in a counter-intuitive direction (Figure 5).

[37] The uplifted isopycnals in Figure 5a are consistent with the time-mean advection velocities only because the source term Q_ρ is nonzero as a result of the gradients of the eddy fluxes. Because the upward bowed isopycnals, which create the baroclinic pressure gradients that help support the jets via geostrophy, depend on the oscillatory flow, the jets almost surely constitute an example of stratified topographic flow rectification.

[38] *Chen and Beardsley* [1995] attributed the uplifting of isopycnals in their study of Georges Bank to "tidal mixing," but the distinction needs to be made between stirring and mixing. In a model sense, stirring accounts for redistribution by resolved flows, while mixing has to do with redistribution by unresolved flows. In the case of *Chen and Beardsley* [1995], forcing was at the M_2 frequency only, so the effects of all other frequencies had to be imbedded into mixing terms. In the present example, the resolved oscillatory flows cause the uplifted isopycnals, and the unresolved motion/transport (the mixing) makes a relatively tiny contribution to the momentum and property field balances. Moreover, it is the very long period subtidal flows, not those nearer the inertial period, that are shaping the isopycnals over the ridge, results described in two paragraphs to follow. *Chen and Beardsley* [1995] showed that rectified flow around Georges Bank were divided approximately 50–50 between the tidal rectification associated with the nonlinear momentum advection terms and the baroclinic pressure gradients originating with "tidal mixing." *Loder* [1980], using an *unstratified* model, had earlier indicated that the nonlinear momentum advection terms would cause anticyclonic rectified flow around Georges Bank, but the model produced weaker mean flows than those observed. In our EPR 9–10°N example, and after spin-up, the nonlinear momentum advection terms directly influence the time-mean jets only to a distance of ~3–4 km from the ridge crest, with isopycnal uplifting and associated pressure gradients caused by resolved oscillatory motion primarily balancing the time-mean Coriolis force beyond that (Figure 7a).

[39] A remaining issue is which oscillation frequencies are most important to giving the jets the magnitudes that they have. *Zimmerman* [1978], for example, argued that the ratio of the excursion distance of the oscillatory flow to the topographic length is an important factor in the strength of rectification, with the larger excursion distances leading to larger rectified flows. Using the spectrum of zonal currents measured over the ridge crest, cross-ridge excursion distances were calculated as the product of spectral amplitude and period of oscillation. That result shows that the envelope of excursion distances rise approximately exponentially over the oscillation period interval 10 to 127 days by 2 orders of magnitude. To evaluate which frequency components most influenced jet size and strength, three additional calculations were conducted in which different truncated subinertial frequency ranges were used. The three experiments limited forcing oscillations to periods $T < 10$ d, $T < 30$ d, and $T < 90$ d. The consequences for the yearly mean jets are depicted in Figure 11. The instantaneous fields, e.g., the IW (Figure 2) and turbulent intensity fields, look very much alike in all experiments because so much of the incident energy in the forcing is in the super-inertial range.

[40] When oscillations with periods $T \geq 10$d, $T \geq 30$d, and $T \geq 90$d were removed from the forcing spectra (Figure 11), the paired (maxima, minimum) jet magnitudes were reduced from (4.6,–4.0) cm s^{-1} in the base case to (1.4, −1.5), (3.2, −2.7), and (4.6, −3.9) cm s^{-1}, respectively. Figure 11 shows that with decreasing subinertial power in the forcing, the jets increasingly lose width as well as height and depth to which the jets influence along-ridge flow. The loci of the velocity maxima move upward on the flanks, so that with little subinertial forcing the jets' velocity extrema (Figure 11a) are located at ridge-crest depth. Examination of the force balance analogous to Figure 7 (not shown) shows that the nonlinear momentum advection terms have elevated importance over 5–6 km from the ridge in cases where oscillations with $T > 10$ d have been eliminated, implying that the isopycnal doming is weaker when weaker long-period forcing is involved. The correlation of the depth of the velocity maxima with forcing period is analogous to results of an analytic model examining subinertial wave trapping around a seamount [e.g., *Lavelle and Cannon*, 2001]. They show that the longer the period of the incident wave on the seamount, the lower along its flanks the center of that trapped wave is found.

4. Conclusions-Summary

[41] Anticyclonic mean-flow jets trapped to the flanks of the EPR 9–10°N seem likely the result of stratified topographic flow rectification. Within a few kilometers of the ridge crest, nonlinear momentum advection and baroclinic pressure gradient terms balance the Coriolis term in the across-ridge equation of motion for yearlong mean flow.

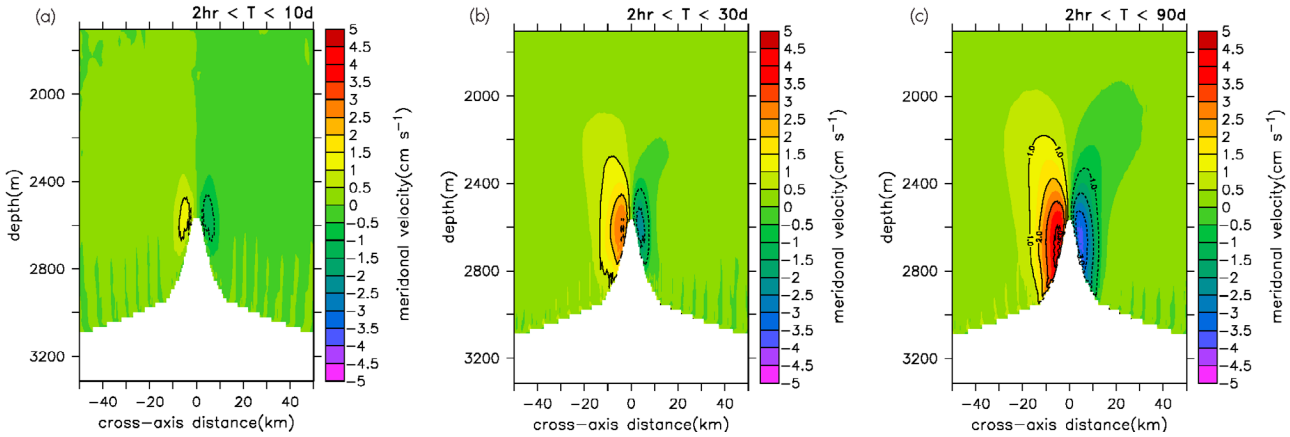

Figure 11. Yearlong mean along-ridge currents for cases where the forcing includes only oscillation periods T where (a) T < 10 d, (b) T < 30 d, and (c) T < 90 d. Line contours are in whole number cm s^{-1}.

Beyond that distance, the force balance is primarily between Coriolis and baroclinic pressure gradients, making the balance geostrophic. The pressure gradients underlying that geostrophy owe their existence to domed isopycnals, and the domed isopycnals are the consequence of the nonzero gradients of time mean of cross-correlations of oscillating currents and hydrographic fields, i.e., divergences of eddy momentum and eddy property fluxes. Both depend on oscillatory flows. Because the 2-d model used here assumes along-ridge invariance of variables, it excludes the possibility of other mechanisms (e.g., as in *Haidvogel and Brink* [1986]), as noted earlier, from contributing to along-isobath mean flow. If those mechanisms are ultimately shown to be significant, the inference here that long period oscillations are likely the primary agents of jet formation at deep ocean ridges will have to be re-assessed.

[42] Numerical experimentation confirms that the strength and planar (x–y) extent of the jets, in the context of this model, depends on the subinertial content of the forcing time series, oscillations whose origins are not considered here. Long-period flows widen and deepen the jets. The base experiment using actual EPR flows show the strong time dependence of jet features. Associated with the jets is a small downward current over the ridge crest that crosses upwardly concave time-mean isopycnals in a counter-intuitive direction. This nonzero time-mean diapycnal advective transport of fields is ultimately caused by a source-like term in the density transport equation, once again associated with gradients of the time-mean product of out-of-phase current and hydrographic oscillations. The importance of the subinertial components in these results argues for a full spectrum of oscillatory flow in forcing numerical models of ocean flow near topographic features. Because jets of the kind measured and modeled at the EPR may represent a significant stirring mechanism for abyssal flow and because they can be important agents of biological transport in the deep, large-scale ocean models that cannot resolve features the size of the jets or account for them in other ways [e.g., *Merryfield and Scott*, 2007] may be overlooking abyssal stirring/transport mechanisms of importance.

[43] **Acknowledgments.** This work was funded by NOAA's Pacific Marine Environmental Laboratory and by NOAA's Vents Program. I thank Dennis McGillicuddy Jr. and Jim Ledwell for questions leading to this analysis, Andreas Thurnherr for providing the LADDER current time series and hydrographic profiles used in the examples, and two anonymous reviewers for their suggestions which improved the text. The freeware application Ferret was used to analyze and display model results. This is contribution 3724 from NOAA's Pacific Marine Environmental Laboratory.

References

Adams, D. K. (2007), Influence of hydrodynamics on the larval supply to hydrothermal vents on the East Pacific Rise, PhD thesis, Mass. Inst. of Technol., Cambridge.

Adams, D. K., D. J. McGillicuddy Jr., L. Zamudio, A. M. Thurnherr, X. Liang, O. Rouxel, C. R. German, and L. S. Mullineaux (2011), Surface-generated mesoscale eddies transport deep-sea products from hydrothermal vents, *Science*, *332*(6029), 580–583, doi:10.1126/science.1201066.

Adcroft, A. J., C. N. Hill, and J. Marshall (1997), Representation of topography by shaved cells in a height coordinate ocean model, *Mon. Weather Rev.*, *125*, 2293–2315, doi:10.1175/1520-0493(1997)125<2293:ROTBSC>2.0.CO;2.

Andersson, H. C., and G. Veronis (2004), Thermohaline circulation in a two-layer model with sloping boundaries and a mid-ocean ridge, *Deep Sea Res., Part I*, *51*(1), 93–106, doi:10.1016/j.dsr.2003.09.011.

Beckmann, A., and D. B. Haidvogel (1997), A numerical simulation of flow at Fieberling Guyot, *J. Geophys. Res.*, *102*(C3), 5595–5613, doi:10.1029/96JC03414.

Bretherton, F. P., and D. B. Haidvogel (1976), Two-dimensional turbulence above topography, *J. Fluid Mech.*, *78*, 129–154, doi:10.1017/S002211207600236X.

Brink, K. H. (1989), The effect of stratification on seamount-trapped waves, *Deep Sea Res., Part A*, *36*(6), 825–844, doi:10.1016/0198-0149(89)90031-9.

Brink, K. H. (1995), Tidal and lower frequencies above Fieberling Guyot, *J. Geophys. Res.*, *100*(C6), 10,817–10,832, doi:10.1029/95JC00998.

Brink, K. H. (2010), Topographic rectification in a forced, dissipative, barotropic ocean, *J. Mar. Res.*, *68*(3–4), 337–368, doi:10.1357/002224010794657209.

Cannon, G. A., and D. J. Pashinski (1997), Variations in mean currents affecting hydrothermal plumes on the Juan de Fuca Ridge, *J. Geophys. Res.*, *102*, 24,965–24,976, doi:10.1029/97JC01910.

Cannon, G. A., and R. E. Thomson (1996), Characteristics of 4-day oscillations trapped by the Juan de Fuca Ridge, *Geophys. Res. Lett.*, *23*(13), 1613–1616, doi:10.1029/96GL01370.

Cannon, G. A., D. J. Pashinski, and M. R. Lemon (1991), Middepth flow near hydrothermal venting sites on the southern Juan de Fuca Ridge, *J. Geophys. Res.*, *96*, 12,815–12,831, doi:10.1029/91JC01023.

Chen, C., and R. C. Beardsley (1995), A numerical study of stratified tidal rectification over finite-amplitude banks: Part 1, Symmetrical banks, *J. Phys. Oceanogr.*, *25*(9), 2090–2110, doi:10.1175/1520-0485(1995)025<2090:ANSOST>2.0.CO;2.

Chen, C., R. Beardsley, and P. J. S. Franks (2001), A 3-D prognostic numerical model study of the Georges Bank ecosystem. Part I: Physical model, *Deep Sea Res., Part II*, *48*(1–3), 419–456, doi:10.1016/S0967-0645(00)00124-7.

Crane, K., F. Aikman, R. W. Embley, S. R. Hammond, A. Malahoff, and J. Lupton (1985), The distribution of geothermal fields on the Juan de Fuca Ridge, *J. Geophys. Res.*, *90*(B1), 727–744, doi:10.1029/JB090iB01p00727.

Garreau, P., and R. Mazé (1992), Tidal rectification and mass transport over a shelf break: A barotropic frictionless model, *J. Phys. Oceanogr.*, *22*, 719–731, doi:10.1175/1520-0485(1992)022<0719:TRAMTO>2.0.CO;2.

Garrett, C., and E. Kunze (2007), Internal tide generation in the deep ocean, *Annu. Rev. Fluid Mech.*, *39*, 57–87, doi:10.1146/annurev.fluid.39.050905.110227.

Haidvogel, D. B., and K. H. Brink (1986), Mean currents driven by topographic drag over the continental shelf and slope, *J. Phys. Oceanogr.*, *16*(12), 2159–2171, doi:10.1175/1520-0485(1986)016<2159:MCDBTD>2.0.CO;2.

Helfrich, K. R., T. M. Joyce, G. A. Cannon, S. A. Harrington, and D. J. Pashinski (1998), Mean hydrographic and velocity sections near Pipe Organ vent at Juan de Fuca Ridge, *Geophys. Res. Lett.*, *25*, 1737–1740, doi:10.1029/98GL01308.

Huthnance, J. M. (1973), Tidal current asymmetries over the Norfolk Sand Bank, *Estuarine Coastal Shelf Sci.*, *1*, 89–99.

Imasato, N. (1983), What is tide-induced residual current?, *J. Phys. Oceanogr.*, *13*(7), 1307–1317, doi:10.1175/1520-0485(1983)013<1307:WITIRC>2.0.CO;2.

Lavelle, J. W. (2006), Flow, hydrography, turbulent mixing, and dissipation at Fieberling Guyot examined with a primitive equation model, *J. Geophys. Res.*, *111*, C07014, doi:10.1029/2005JC003224.

Lavelle, J. W., and G. A. Cannon (2001), On subinertial oscillations trapped by the Juan de Fuca Ridge, northeast Pacific, *J. Geophys. Res.*, *106*(C12), 31,099–31,116, doi:10.1029/2001JC000865.

Lavelle, J. W., and C. Mohn (2010), Motion, commotion, and biophysical connections at deep ocean seamounts, *Oceanography*, *23*(1), 90–103, doi:10.5670/oceanog.2010.64.

Lavelle, J. W., and W. C. Thacker (2008), A pretty good sponge: Dealing with open boundaries in limited-area ocean models, *Ocean Modell.*, *20*(3), 270–292, doi:10.1016/j.ocemod.2007.10.002.

Lavelle, J. W., A. M. Thurnherr, J. R. Ledwell, D. J. McGillicuddy, and L. S. Mullineaux (2010), Deep ocean circulation and transport where the East Pacific Rise at 9–10°N meets the Lamont seamount chain, *J. Geophys. Res.*, *115*, C12073, doi:10.1029/2010JC006426.

Loder, J. W. (1980), Topographic rectification of tidal currents on the sides of Georges Bank, *J. Phys. Oceanogr.*, *10*, 1399–1416, doi:10.1175/1520-0485(1980)010<1399:TROTCO>2.0.CO;2.

Maas, L. R. M., and J. T. F. Zimmerman (1989), Tide-topography interactions in a stratified shelf sea, part I. Basic equations for quasi-nonlinear internal tides, *Geophys. Astrophys. Fluid Dyn.*, *45*(1–2), 1–35, doi:10.1080/03091928908208891.

Mahadevan, A. (2006), Modeling vertical motion at ocean fronts: Are nonhydrostatic effects relevant at submesoscales?, *Ocean Modell.*, *14*, 222–240, doi:10.1016/j.ocemod.2006.05.005.

McGillicuddy, D. J., Jr., J. W. Lavelle, A. M. Thurnherr, V. K. Kosnyrev, and L. S. Mullineaux (2010), Larval dispersion along an axially symmetric mid-ocean ridge, *Deep Sea Res., Part I*, *57*(7), 880–892, doi:10.1016/j.dsr.2010.04.003.

Merryfield, W. J., and R. B. Scott (2007), Bathymetric influence on mean currents in two-high resolution near-global models, *Ocean Modell.*, *16*, 76–94, doi:10.1016/j.ocemod.2006.07.005.

Mohn, C., M. White, I. Bashmachnikov, F. José, and J. L. Pelegrí (2009), Dynamics at an elongated, intermediate depth seamount in the North Atlantic (Sedlo Seamount, 40°20′N, 26°40′W), *Deep Sea Res., Part II*, *56*(25), 2582–2592, doi:10.1016/j.dsr2.2008.12.037.

Morse, P., and H. Feshbach (1953), *Methods of Theoretical Physics*, vol. 1, 997 pp., McGraw-Hill, New York.

Müller, P. (1995), Ertel's potential vorticity theorem in physical oceanography, *Rev. Geophys.*, *33*(1), 67–97, doi:10.1029/94RG03215.

Ou, H.-W. (1999), A model of tidal rectification by potential vorticity mixing. Part 1: Homogeneous ocean, *J. Phys. Oceanogr.*, *29*, 821–827, doi:10.1175/1520-0485(1999)029<0821:AMOTRB>2.0.CO;2.

Pérenne, N., A. Pichon, and P. Huet (2000), A numerical study of stratified tidal rectification, *Cont. Shelf Res.*, *20*(1), 37–68, doi:10.1016/S0278-4343(99)00057-6.

Robinson, I. S. (1981), Tidal vorticity and residual circulation, *Deep Sea Res., Part A*, *28*(3), 195–212.

Shen, Y., and K. R. Thompson (1997), Oscillating flow of a homogeneous fluid over an isolated topographic feature, *Atmos. Ocean*, *35*(3), 229–255, doi:10.1080/07055900.1997.9649593.

Smagorinsky, J. (1993), Some historical remarks on the use of nonlinear viscosities, in *Large Eddy Simulation of Complex Engineering and Geophysical Flows*, edited by B. Galperin and S. A. I. Orsag, pp. 3–36, Cambridge Univ. Press, New York.

Tee, K. T. (1976), Tide-induced residual currents, a 2-D nonlinear numerical tidal model, *J. Mar. Res.*, *34*, 603–628.

Thomson, R. E., S. E. Roth, and J. Dymond (1990), Near-inertial motions over a mid-ocean ridge: Effects of topography and hydrothermal plumes, *J. Geophys. Res.*, *95*(C5), 7261–7278, doi:10.1029/JC095iC05p07261.

Thurnherr, A. M., J. R. Ledwell, J. W. Lavelle, and L. S. Mullineaux (2011), Hydrography and circulation near the crest of the East Pacific Rise between 9° and 10°N, *Deep Sea Res., Part I*, *58*(4), 365–376, doi:10.1016/j.dsr.2011.01.009.

Vallis, G. K., and M. E. Maltrud (1993), Generation of mean flows and jets on a beta-plane and over topography, *J. Phys. Oceanogr.*, *23*(7), 1346–1362, doi:10.1175/1520-0485(1993)023<1346:GOMFAJ>2.0.CO;2.

Zaron, E. D., and G. D. Egbert (2006), Verification studies for a z-coordinate primitive equation model: Tidal conversion at a mid-ocean ridge, *Ocean Modell.*, *14*, 257–278, doi:10.1016/j.ocemod.2006.05.007.

Zimmerman, J. T. F. (1978), Topographic generation of residual circulation by oscillatory (tidal) currents, *Geophys. Astrophys. Fluid Dyn.*, *11*, 35–47, doi:10.1080/03091927808242650.

Zimmerman, J. T. F. (1980), Vorticity transfer by tidal currents over an irregular topography, *J. Mar. Res.*, *38*(4), 601–630.